Unsteady Lattice Boltzmann Simulations of Corner Separation in a Compressor Cascade

J. Boudet, E. Lévêque, H. Touil

Unsteady lattice Boltzmann simulations of corner separation in a compressor cascade

J. Boudet* and E. Lévêque

Univ Lyon, Ecole Centrale de Lyon, CNRS, Univ Claude Bernard Lyon 1,

INSA Lyon,

LMFA, UMR 5509, F-69130, Ecully, France

* jerome.boudet@ec-lyon.fr

H. Touil

CS-group France, Lyon

July 22, 2021

Abstract

Lattice-Boltzmann simulations of corner separation flow in a compressor cascade are presented. The lattice Boltzmann approach is rather new in the context of turbomachinery and the configuration is known to be particularly challenging for turbulence modelling. The present methodology is characterized by a quasi-autonomous meshing strategy and a limited computational cost (a net ratio of 5 compared to a previous finite-volume compressible Navier-Stokes simulation). The simulation of the reference case (4° incidence) shows a good agreement with the experimental data concerning the wall pressure distribution or the distribution of losses. A good description is also obtained when incidence angle is increased to 7°, with a span-wise development of the separation. Subsequently, the methodology is used to investigate the sensitivity of the flow to the end-wall boundary-layer thickness. A thinner boundary-layer results in a smaller corner separation, but not a

complete elimination. Finally, the ingredients of the wall modelling are analysed in details. On the one hand, the curvature correction term promotes transition to turbulence on the blade suction side and avoids a spurious separation. On the other hand, the addition of the pressure-gradient correction term allows a wider and more realistic corner separation.

Keywords: lattice-Boltzmann method, corner separation, compressor cascade.

1 Introduction

Flows in the compression stages of jet engines are particularly complex, i.e. three-dimensional, unsteady and highly turbulent. In addition, an adverse pressure gradient makes them prone to separate. Consequently, particular attention must be paid to the design of these components to optimize the efficiency and the operating range of the jet engine. Nowadays, the design of the flow-path relies heavily on flow simulations, which need to be both accurate and affordable in terms of computational cost, despite the great complexity of the flow.

The present study focuses on a specific, and particularly delicate phenomenon: the *corner separation* that occurs at the junction between the blade suction side and an end-wall (hub or casing). The combination of the respective boundary layers, and the pressure gradient, tend to create a three-dimensional separation that affects the performance (efficiency and stability) of the component. The phenomenon of corner separation has been analysed in a linear cascade experiment, representative of a compressor geometry, at Ecole Centrale de Lyon. Various studies have been conducted on this configuration, including the experimental work by Zambonini *et al.* [1], to which the present lattice Boltzmann results will be compared. A Navier-Stokes wall-resolved large-eddy simulation (LES) has also been performed by Gao *et al.* [2] with results found in good agreement with the experiment. Gao *et al.* [3] also analysed the fidelity of (much cheaper) Reynolds-averaged Navier-Stokes (RANS) simulations based on many different turbulence models, and showed they all failed to capture the correct extent of the corner separation. So confirming that this configuration is a challenging test case for computational fluid dynamics (CFD). An interesting compromise has been proposed by Xia *et al.* [4], who employed a hybrid RANS-LES strategy (delayed detached eddy simulation) and obtained fairly good results on the same configuration. Some discrepancies were still visible on the contours

of total pressure losses, but the prediction was much better than with RANS and for a moderate computational cost.

The lattice Boltzmann (LB) method has recently emerged as a conceptually different approach to CFD; the first computationally viable achievement dates back to the late 80s [5]. While conventional methods rely on the macroscopic equations of fluid mechanics, the LB method addresses fluid motions at an underlying mesoscopic level. Capturing the statistical behaviour of collections of particles evolving on a regular lattice is here preferred to solving non-linear partial differential equations. This is made possible because most details at the mesoscopic level play actually no role in the macroscopic dynamics. Therefore, fairly simple kinetic equations can be devised. A major advantage of the LB method is that it leads to algorithms that can be executed very efficiently on parallel computers, thus offering the promise of complex turbulent-flow simulations with advantageous execution times. Another positive point is that non trivial meshing strategy near boundary can be avoided by resorting to immersed boundary conditions realizable for any arbitrary geometry. The use of the LB method in engineering applications is gaining maturity and begins to challenge traditional Navier-Stokes methods [6]. Our study examines quantitatively the potential of the LB approach (in terms of accuracy and turnaround time) on a configuration of particular interest in the domain of turbomachinery flows, namely, the corner separation in a compressor cascade.

Recently, Maros *et al.* [7] have independently presented LB results related to the compressor cascade configuration from Ecole Centrale de Lyon investigated in the present article. They showed promising results for the reference case, i.e. for a single boundary-layer thickness and a single angle of incidence. The objective of the present article, beyond reproducing the simulation of the reference case with a different solver and presenting complementary analyses, is also to investigate the sensitivity of the prediction to the flow parameters, and to detail and examine the physical ingredients of the wall modelling.

The setup of the lattice Boltzmann simulation is introduced in section 2. The results obtained for an angle of incidence $i = 4°$ (reference case) are presented in section 3 and compared with available data from the experiment and the literature. Finally, in section 4, the sensitivity of the corner separation is examined against the incidence angle and the thickness of the end-wall boundary layer. The ingredients of wall modelling used to account for (unresolved) near-wall dynamics are also examined more closely.

2 Numerical methods

The lattice Boltzmann simulations have been performed with the industrial ProLB solver (www.prolb-cfd.com) developed within a scientific collaboration including CS-group France, Renault, Airbus, Ecole Centrale de Lyon, CNRS and Aix-Marseille University. To alleviate computational efforts, the smallest turbulent scales of motion – the most computationally expensive – are ignored. Therefore, fluid dynamics is investigated within the framework of "Wall-Modelled Large-Eddy Simulation" that resorts to a wall function (or wall law) in the vicinity of solid boundaries and a subgrid turbulent viscosity in the bulk of the flow [8]. These numerical ingredients are now introduced.

2.1 Lattice Boltzmann scheme

In the LB framework, macroscopic variables such as the density or the fluid momentum are obtained from the statistical moments

$$\rho(\mathbf{x},t) = \sum_{i=0}^{N-1} f_i(\mathbf{x},t) \quad \text{and} \quad \rho\mathbf{u}(\mathbf{x},t) = \sum_{i=0}^{N-1} f_i(\mathbf{x},t)\mathbf{c_i} \tag{1}$$

where the distribution functions $f_0(\mathbf{x},t), \cdots, f_{N-1}(\mathbf{x},t)$ are associated with a *discrete* set of microscopic velocities $\mathbf{c_0}, \cdots, \mathbf{c_{N-1}}$. The sums replace here the integrals over all possible microscopic velocities in the classical kinetic theory of gases [9]. In brief, this discretization stems from expanding and truncating the solution of the original continuum Boltzmann equation onto a finite basis of tensorial Hermite polynomials in velocity, and resorting to Gaussian quadrature formula to approximate statistical moments [10, 11]. Therefore, the f_i's evolve according to a discrete-velocity analogue of the Boltzmann equation that is eventually discretized in space and time to yield the LB scheme.

The set of velocities $\mathbf{c_0}, \cdots, \mathbf{c_{N-1}}$ determines the lattice. In our solver, the discretization in velocity refers to a D3Q19 cubic lattice (see Fig. 1) with 19 possible velocities at each node. The LB algorithm advances in time the f_i's on the lattice and proceeds in a two-step *collide-and-stream* procedure. The collision is local and performs the instantaneous redistribution of particles among the different microscopic velocities:

$$f_i^{\text{out}}(\mathbf{x},t) = f_i(\mathbf{x},t) + \Omega_i(\mathbf{x},t) \quad \text{for } i = 0,\ldots,N-1 \tag{2}$$

where Ω_i refers to the collision operation. The streaming step is consecutive to the collision and transports the particles according to their post-collision velocity to a neighbouring lattice node, i.e.

$$f_i(\mathbf{x} + \mathbf{c_i}\Delta_t, t + \Delta_t) = f_i^{\text{out}}(\mathbf{x}, t). \tag{3}$$

The flow complexity emerges from the repetition of these simple rules operating at each timestep at each node of the lattice.

Importantly, fluid mechanics is introduced through the modelling of the collision operator. In this respect, the so-called BGK approximation [12] is generally used with

$$\Omega_i^{\text{BGK}}(\mathbf{x}, t) = -\frac{1}{\tau_S}\left(f_i(\mathbf{x}, t) - f_i^{\text{eq}}(\mathbf{x}, t)\right). \tag{4}$$

Therefore, all distribution functions relax towards their values at absolute equilibrium with a unique relaxation coefficient $\tau_S = 1/2 + \nu/c_s^2\Delta_t$ that relates to the kinematic shear viscosity of the fluid (ν) and the speed of sound (c_s). The equilibrium distributions f_i^{eq} are given by the truncated Hermite expansion of the continuous Maxwell-Boltzmann distribution. The truncation is usually made at second order with

$$f_i^{\text{eq}} \simeq w_i\rho\left\{1 + \frac{c_{i\alpha}u_\alpha}{c_s^2} + \frac{u_\alpha u_\beta\, Q_{i\alpha\beta}}{2c_s^4} + \cdots\right\} \quad \text{with} \quad Q_{i\alpha\beta} = c_{i\alpha}c_{i\beta} - c_s^2\delta_{\alpha\beta} \tag{5}$$

where the weighting coefficients are given by $w_0 = 1/3$, $w_{1\ldots6} = 1/18$ and $w_{7\ldots18} = 1/36$ for the D3Q19 lattice ; the summation on the repeated Cartesian coordinates α and β is implicit (Einstein notation). This approximation is sufficient to ensure that the macroscopic solution satisfies the weakly-compressible Navier-Stokes equations with third-order corrections in Mach number [10]. Compressibility is taken into account by the simple equation of state $p = \rho c_s^2$ which is justified in the low-Mach regime ; relative fluctuations of density are $\mathcal{O}(\text{Ma}^2)$. Finally, let us mention that the timestep is bound to the lattice spacing by

$$\frac{\Delta_x}{\Delta_t} = \sqrt{3}c_s \tag{6}$$

so that particles move from a lattice node to another lattice node during exactly one time step.

Although the BGK scheme is generally considered as the orthodox LB scheme, it suffers from severe stability issues in the zero-viscosity limit unless the lattice spacing is

dramatically reduced. In order to address highly turbulent flows, a variant of the standard BGK scheme has been here adopted for better stability and robustness. It is based on a two-relaxation-time collision operator supplemented with high-order selective filters applied to flow variables [13]. The idea behind this variant is to artificially over-relax the distributions towards equilibrium to improve the stability [14, 15] while preserving the conservation of mass and momentum. The correct nonequilibrium part of the distributions (which encompasses dissipative dynamics) is recovered through a second-order regularization procedure [16]. This modified collision expresses as

$$\Omega_i^{\mathrm{DRT}} = -\frac{1}{\tau_N}\left(f_i(\mathbf{x},t) - f_i^{\mathrm{eq}}(\mathbf{x},t)\right) + \frac{\tau_S - \tau_N}{\tau_N \tau_S}\frac{w_i}{2c_s^4}\,\Pi_{\alpha\beta}^{\mathrm{neq}}\,Q_{i\alpha\beta} \tag{7}$$

where $\Pi_{\alpha\beta}^{\mathrm{neq}} = \sum_i (f_i - f_i^{\mathrm{eq}}) c_{i\alpha} c_{i\beta}$ is the second-order non-equilibrium moment and the artificial relaxation coefficient $\tau_N = 0.55$ [15].

2.2 Wall-Modelled Large-Eddy Simulation

2.2.1 Wall law

The LB scheme requires to specify the distribution functions at boundary nodes (i.e. first off-wall fluid nodes). Due to the presence of the wall, boundary nodes lack neighbours and distributions can not be updated by simply streaming the distributions from the neighbouring nodes. An alternative method must be called. Bounced-back rules are often used in the presence of straight walls or for moderate curvature [17]. Here, the adopted method relies on a reconstruction of particle distributions from macroscopic flow variables (mass density and velocity). The method accounts accurately for the curvature of the boundary [18, 19].

When the lattice is sufficiently fine to resolve the boundary-layer dynamics, the density is obtained from a zero-normal-pressure-gradient condition at the wall (homogeneous Neumann condition), whereas the velocity is inferred from an interpolation satisfying an homogeneous Dirichlet boundary condition. In the context of industrial turbulent flows around complex geometries, the resolution of boundary layers is usually not affordable. In that situation, a wall law can be used to match the flow variables at the first off-wall fluid node with the unresolved boundary-layer dynamics [20]. This wall law is calibrated by using second off-wall fluid nodes (in the interior of the fluid domain).

This is the approach developed in the ProLB solver. An analytic wall function (described below) is used to force explicitly the wall parallel components of the velocity at boundary nodes. The relevance of this modelling is examined in section 4.

For a turbulent boundary layer over a flat plate, the classical log law (in the logarithmic layer) writes

$$U_0^+(y^+) \,=\, \frac{1}{\kappa}\,\log\left(y^+\right) \,+\, B \tag{8}$$

where U_0^+ and y^+ denote respectively the velocity and the distance to the boundary in wall units[1]. The so-called von Kármán constant and the constant B take the values $\kappa = 0.41$ and $B = 5.2$. [8].

This law is here generalized as

$$U^+(y^+) = \left(U_0^+(y^+) \,+\, F_c(y^+) \,+\, F_p(y^+)\right) \cdot F_d(y^+) \tag{9}$$

where $F_c(y^+)$, $F_p(y^+)$ and $F_d(y^+)$ represent corrections accounting respectively for the curvature of the boundary, the pressure gradient and the near-wall damping. The curvature correction writes in agreement with [21]

$$F_c(y^+) \,=\, (\alpha K^+ y^+)\,\{U_0^+ \,-\, \frac{1}{\kappa}\} \,+\, \mathcal{O}\left((K^+ y^+)^2\right) \tag{10}$$

where the curvature is defined as $K \,=\, 1/R$ with R being the radius of curvature of the surface in the streamwise direction[2]. The parameter $\alpha \,=\, 6$ belongs to the range recommended by Patel & Sotiropoulos [21]. The pressure-gradient correction is defined in agreement with [22, 23] as

$$F_p(y^+) \,=\, \frac{1}{\kappa}\,\left[-2\,\log\left(\frac{\sqrt{1+\Pi^+ y^+}+1}{2}\right) + 2\,\left(\sqrt{1+\Pi^+ y^+}-1\right)\right] \tag{11}$$

with $u_p \,=\, \left(\frac{\nu}{\rho}\frac{\partial P}{\partial x}\right)^{\frac{1}{3}}$ and $\Pi^+ \,=\, \left(\frac{u_p}{u_w}\right)^3$. The parameter B in Eq. (8) can no longer be considered as constant in the presence of a pressure gradient [23]. An empirical approxi-

[1] $U_0^+ = \frac{U_0}{u_w}$ and $y^+ = \frac{y\,u_w}{\nu}$ with u_w and ν being the friction velocity at the wall and the kinematic viscosity of the fluid, respectively.

[2] $K^+ = \frac{K\,\nu}{u_w}$.

mation of B as a function of Π^+ is given by

$$B(\Pi^+) \;=\; 1.0 \;+\; (B_0 - 1.0)\,\exp\left(-\left(\frac{\Pi^+}{C_B}\right)^2\right) \tag{12}$$

where $B_0 = 5.2$ is the value in absence of pressure gradient (flat plate) and $C_B \simeq 0.05$ [23].

A median value $B = 3$ between $B(\infty)$ and $B(0)$ is taken in our solver instead of the full parametrization.

Finally, the near-wall damping correction writes

$$F_d(y^+) = \left(1 - \exp(-\frac{y^+}{C_d})\right) \tag{13}$$

with the parameter $C_d = 8$. This damping allows a consistent closure for $y^+ \lesssim 25$. This is motivated by the fact the value of y^+ cannot be finely controlled with a Cartesian grid on curved walls.

In summary, the generalized wall law Eq. (9) including curvature, pressure gradient and near-wall corrections is calibrated from second off-wall fluid nodes in the wall-normal direction, and used to predict the velocity at first off-wall boundary nodes [24]. Concerning the density, the homogeneous Neumann condition is still used by assuming the pressure remains almost constant in the wall-normal direction.

2.2.2 Subgrid turbulent viscosity

A common thread to account for the unresolved turbulent dynamics in the bulk of the flow is to include an additional subgrid viscosity.

In this regard, a refinement of the classical Smagorinsky's subgrid viscosity is here used to account explicitly for the presence of persistent shear motions, e.g. near a solid boundary or in the near wake of an obstacle. Namely, the Shear-Improved Smagorinsky's model (SISM) relies on the exact scale-by-scale energy budget of fluid turbulence [25] and writes

$$\nu_{\text{sism}}(\mathbf{x}, t) = (C_s \Delta_x)^2 \cdot (|S|(\mathbf{x}, t) - \mathcal{S}(\mathbf{x}, t)) \tag{14}$$

where $C_s = 0.18$ is the standard Smagorinsky's constant, Δ_x is the local lattice spacing and $|S| = \sqrt{2\ S_{ij} S_{ij}}$ denotes the norm of the rate-of-strain tensor [8]. The correcting term $\mathcal{S}$ is the norm of the low-pass filtering (in time) of the rate of strain, as detailed

in [26]. This modelling in conjunction with the LB approach has already proved to be valuable for the simulation of complex turbulent flows [14].

LES is handled straightforwardly within the LB framework. In practice, the subgrid turbulent viscosity appears as an additional contribution to the relaxation coefficient, so that

$$\tau_S(\mathbf{x},t) = \frac{1}{2} + \frac{\nu + \nu_{\rm sism}(\mathbf{x},t)}{c_s^2 \Delta_t}. \tag{15}$$

This value of $\tau_S(\mathbf{x},t)$ is updated at each lattice node prior the collision step; the velocity gradients in Eq. (14) are estimated by second-order central differences. Finally, let us mention that the solver handles multi-domain grid encompassing various levels of refinement in order to optimize the computational cost. The equilibrium distributions match at the interface between adjacent blocks with different resolutions, but the non-equilibrium components, which carry information about the viscous stress, differ. The rescaling of the rate of strain is handled by prolongation and restriction operations, whereas the rescaling of the subgrid-scale viscosity relies on a Kolmogorov similarity argument. The whole procedure is detailed in [27].

2.3 Simulation set-up

The blade cascade configuration, investigated experimentally by Zambonini *et al.* [1] at Ecole Centrale de Lyon, is sketched in Fig. 2. The chord-based Reynolds number is $Re_c = 4 \cdot 10^5$ and the inflow Mach number is 0.12. The simulations are carried out in the same conditions.

The computational domain is shown in Fig. 3. In the lateral y-direction, the domain extends over one blade passage with periodic boundary conditions to account for the cascade configuration. In the span-wise z-direction, only one half of the blade is simulated with a frictionless condition at mid-span to represent the symmetry of the experiment. The length (x-direction) of the inlet duct has been adjusted to match the experimental value of momentum thickness for the end-wall boundary layer. On the walls (blade and end-wall), a wall function is used to bridge the viscous and buffer sub-layers in the first off-wall cell [14, 20]. This avoids resolving the innermost part of the boundary layer in contact with the wall. This wall function includes pressure-gradient effects and curvature corrections, as described in the previous section. The wall law is applied everywhere on the walls, without specific treatment for the laminar regions, whose extent is limited. Indeed, rectangular

steps are used to trip transition to turbulence on the end-wall (height: 2 mm, at 113 mm from the inlet) and on both sides of the blades (height: 0.6 mm, at 6 mm from leading edge). On the end-wall, the step allows a rapid development of the turbulent boundary layer. On the blade, the steps model the sandpaper strips present in the experiment (height: 0.3 mm), however, they are thickened to correspond to approximately 3 grid cells and allow a proper transition. The description of the incoming boundary layer will be analysed in section 3.1, and the global influence on the flow of the formulation of the wall function will be investigated in section 4.3. Velocity is imposed at the inlet and pressure is set at the outlet. Absorbing layers are placed at the inlet and outlet to limit reflections. The thickness of the absorbing layers is 0.02 m at the inlet and 0.10 m at the outlet, corresponding respectively to 0.13 and 0.67 chord lengths. The Shear-Improved Smagorinsky model Eq. (14) is used to account for strong shear effects associated with attached or separated boundary-layers [25].

Concerning the octree grid, four resolution levels are defined with an edge growth ratio of two between consecutive levels [27]. Near walls, the finest resolution (level 1) is used with grid spacing $\Delta_x = 2.1 \cdot 10^{-4}$ m corresponding to $\Delta_x^+ \approx 20$ in wall units. Then, resolution progressively reduces to level 4 away from the walls. An illustration of the grid around the leading edge at mid-span is shown in Fig. 4. The first three levels are visible in this figure. The steps near the leading edge are the tripping bands. Around the corner separation region, for $-0.27 \leq x/c_a \leq 1.54$ and $z/h \leq 0.36$, level 2 resolution is maintained for a uniform and refined resolution. The total number of nodes is about $107 \cdot 10^6$. The time step is $\Delta_t = 3.5 \cdot 10^{-7}$ s at the finest resolution level, and the simulation is run for 500 000 iterations. The calculation of the flow statistics uses the last 200 000 iterations, corresponding to approximatively $19c/U_0$. Simulation is parallelized on 192 CPU cores and the total computational cost is $16 \cdot 10^3$ CPUh per simulation corresponding to 83 hours on wall clock.

In comparison, the wall-resolved compressible finite-volume simulation performed by Gao *et al.* [2] required $2 \cdot 10^6$ CPUh for a shorter duration ($\sim 19c/U_0$ instead of $47c/U_0$ in total). The raw speed-up factor is approximately 300 with the present LB approach for the same physical duration, which makes it much more adapted to parametric investigations. However, this speed-up results from two main differences: (i) the wall function allows a coarser meshing at wall, the time step is thus increased and the total number of grid points

is reduced, (ii) a "low Mach-number" LB approach is employed instead of the compressible finite-volume approach. The speed-up induced by (i) can be estimated by the ratio of the minimum cell sizes multiplied by the ratio of the total number of grid points, which yields a factor of around 60. Consequently, the numerical approach (ii) yields a net speed-up of about 5. Note that this evaluation of the speed-up remains indicative and rough since some aspects are not considered, e.g. the time integration methodology. Also, while the finite-volume methodology used by Gao *et al.* is readily adapted to high Mach-number flows, the present LB methodology requires adaptations to simulate such flow conditions. This is of major interest in the context of turbomachinery flows, but, this has not been evaluated in the present work.

3 Results for the reference incidence angle ($i = 4°$)

The flow topology in the reference case is illustrated in Fig. 5. First, the mean flow is shown in the left image. The computational domain is repeated pitchwise for visualization purpose but only one blade passage is simulated. The friction lines show the corner separation that develops on both the end-wall and the blade suction side, near trailing edge. This is the mechanism of interest. A local separation is also visible near the leading edge, induced by the tripping band. The total pressure loss coefficient is plotted in 'section 1', downstream of the blade, and will be analyzed in section 3.5. The wake of the blade (vertical band) and the wake of the corner separation (triangular region) are clearly visible. The instantaneous flow is shown on the right image, over three blade passages (periodic copies). The Q-criterion iso-surface shows the turbulent eddies transported by the incoming boundary layer on the end-wall, the development of turbulence on the suction side of the blade, and the proliferation of turbulent structures in the corner separation.

3.1 Inflow boundary-layer

First, the inflow boundary-layer is investigated at distance $4.13\,c_a$ upstream of the leading edge (referred to as 'station 2' in [1]), in comparison to experimental data. The global parameters are given in Table 1. It is recalled that the length of the inlet duct has been adjusted to reproduce approximately the experimental value of the momentum thickness. The agreement on the other parameters is more remarkable: the friction, the boundary

layer thickness, the displacement thickness and the shape factor. For the LB simulation, in which the viscous sub-layer is not resolved, the value of u_w is inferred by minimizing the distance between the classical log law (Eq. (8)) and the normalized mean velocity profile in the logarithmic layer (see Fig. 6). The value of the boundary-layer shape factor, H_{12}, confirms turbulence is developed, allowing a good estimate of the friction velocity.

The mean and fluctuating velocity profiles in the boundary layer are presented in Fig. 6. Concerning the mean velocity, the experimental profile is shown to match the Van Driest law for a turbulent boundary layer. The LB simulation relies on a wall function and does not resolve the viscous sub-layer close to the wall. In these conditions, the log slope is not perfectly rendered, but overall, a fairly good prediction of the external region of the boundary layer is achieved. It is recalled that the u_w value is estimated to best fit the log-law region. Finally, concerning the fluctuating velocity, the experimental profile is less peaky, probably because the experimental boundary layer develops through a longer system of ducts of variable section, and does not correspond to a canonical flat-plate boundary layer. This is consistent with the observations made by Gao [28] on his wall-resolved LES. Apart from this, a fairly good agreement is achieved between the experiment and the LB simulation.

3.2 Blade wall pressure

The mean pressure coefficient on the blade is presented in Fig. 7. The present simulation is compared to the experiment and simulations from the literature, namely, the wall-resolved LES performed by Gao *et al.* [2] and the LB simulation by Maros *et al.* [7] (case with trips).

At $z/h = 29.7\%$ (right-hand side plot), the flow is attached to the blade and is essentially two-dimensional. Lift is generated by the pressure difference between the pressure side (upper curve) and the suction side (lower curve). A fairly good agreement is achieved between the experiment and the different simulations. However, the present simulation shows two imperfections. First, a spurious pressure rise is observed on the suction side, near $x/c_a = 0.2$, probably due to the reattachment of the separated flow downstream of the thickened trip. Second, the numerical curve is also more wiggly, which is probably related to the implementation of the wall boundary condition.

The position $z/h = 1.4\%$ (left-hand side plot) is particularly interesting because it is

close to the end-wall, within the corner separation. On the suction side, the separation is denoted by the stagnation of pressure from $x/c_a \approx 0.5$. Again, the different simulations are in good agreement with the experiment. The present LB simulation is very close to the wall-resolved LES by Gao *et al.*. On the suction side, the global level is more precisely captured by the LB simulation by Maros *et al.*, but not on the pressure side.

3.3 Velocity profiles on suction side

In this section, the mean and fluctuating velocities are investigated along the blade suction side. The positions of the velocity profiles are shown in Fig. 8. First, the spanwise position $z/h = 29.7\%$ is considered. The mean and fluctuating tangential velocities are plotted in Fig. 9. At this spanwise position, the flow is essentially two-dimensional and the boundary layer is attached. From $s^* = 0.21$ to $s^* = 0.99$, the velocity outside of the boundary layer progressively decreases, consistently with the pressure increase on the suction side (see Fig. 7). On the first profile ($s^* = 0.21$), a slight overshoot of mean velocity is observed in the external region of the boundary layer: this is a flaw of the wall-function when applied to a partially turbulent boundary layer, just downstream of the trip. Concerning the fluctuating velocity, the levels achieved in the boundary layer indicate the development of turbulence.

The tangential velocities close to the end-wall, at $z/h = 1.4\%$, are plotted in Fig. 10. The interaction with the end-wall boundary layer results in the corner separation, characterized by negative values of mean tangential velocity from $s^* \approx 0.7$. Accordingly, higher intensities of velocity fluctuations are observed, developing through the blade channel. Far from the blade, the level of fluctuations remains high ($u'/U_{in} \approx 0.1$) because the profiles lie within the end-wall boundary-layer.

3.4 Velocity spectra

Velocity spectra are calculated from two probes located near the end-wall, at distance $\Delta z = 4.95\,\text{mm}$ or $\Delta z^+ \approx 150$. The locations of the probes and the spectra are presented in Fig.11. The orange probe is sufficiently far from the blade, where the end-wall boundary layer is attached. Conversely, the blue probe lies within the corner separation. First, a qualitative observation can be made: the shape of the spectra is classical for a turbulent flow. The content is broadband and the slope is decreasing. The higher levels obtained on

the orange probe indicate that the turbulent kinetic energy (axial component) is stronger in the attached flow. Second, the frequency resolution of the simulation is clearly visible: the cut-off frequency lies around $10\,\mathrm{kHz} = 37.5\,U_0/c$, where the spectrum slope breaks. It is worth mentioning both probes are located in the uniform grid around the separation region (level 2 refinement). The higher frequency resolution achieved on the orange probe comes from the higher velocities at that point, compared to the blue probe in the corner separation.

3.5 Losses

The total pressure loss coefficient is defined as

$$\omega_t = \frac{P_{0in} - P_0}{1/2\rho_{in}U_{in}^2} \tag{16}$$

where P_0 is the stagnation pressure and the subscript 'in' indicates the inflow reference values at 'station 2'.

ω_t is computed on the axial plane 'section 1', located at distance $0.363\,c_a$ downstream of the trailing edge (see Fig. 2). The LB results are compared to the measurements and previous simulations in the first line of Fig. 12. On each plot, two main areas of losses can be identified: the band around $\Delta y/s = 0.2$ is the blade wake, and the triangular region for $z/h < 0.15$ corresponds to the wake of the corner separation.

First, the results from the literature are considered. We observe that the LES by Gao *et al.* [2] is in very good agreement with the experiment. This highly-resolved simulation is considered as a reference. The LB simulation performed by Maros *et al.* [7] gives good results but some discrepancies remain: the blade wake is too thick and the shape of the corner-separation wake differs slightly from the experiment. In comparison, the present LB simulation yields a thinner blade wake, though still slightly thicker than in the experiment. This description of the wake is achieved with a limited resolution of the boundary layer. On the suction side of the blade, at the trailing edge, the grid resolution Δ_x yields $\delta_2/\Delta_x = 8$. Concerning the wake of the corner separation, the shape, the width and the intensity of this region are well captured by the present LB simulation. This agreement between the experiment and the LB simulation is remarkable. Indeed, the prediction of this region is known to be particularly challenging. For example, none of the RANS turbulence models tested by Gao *et al.* [3] managed to predict the wake

of the corner separation, not even the direct Reynolds-stress models (DRSM). In the present simulation, it should be noted that the use of a wall function does not impede the prediction of the corner separation. This suggests that the separation is essentially controlled by the external region of the boundary layers.

4 Sensitivity to flow parameters and wall modelling

In section 3, the present LB methodology was shown to capture the corner separation for the reference incidence angle $i = 4°$. In the present section, the method is further assessed by comparing its sensitivity to the incidence angle against the experiment. Then, the LB methodology is used to evaluate the sensitivity to the incoming boundary-layer thickness, which was not investigated experimentally. Finally, investigations address a crucial modelling aspect: the influence of the different components of the wall function.

4.1 Incidence

Another LB simulation was carried out for an incidence angle $i = 7°$, not available in the numerical studies by Gao *et al.* [2] and Maros *et al.* [7]. The total pressure losses are plotted in Fig. 12 (second line), in comparison with the experiment and the aforementioned results at $i = 4°$ (first line). It appears that the simulation captures the experimental evolution of the corner separation when the incidence increases: the separation wake grows slightly and develops essentially along the blade span. This behavior is natural: the increase of incidence results in a higher blade load, which fosters separation on the suction side. This effect and the moderate amplitude of the evolution are properly captured by the LB simulation.

For a more quantitative comparison, the loss coefficient ω_t is averaged pitchwise:

$$\omega_t^* = \frac{\int_0^s \omega_t \cdot u_x \, dy}{\int_0^s u_x \, dy} \tag{17}$$

The experimental and simulation results, for both angles of incidence, are plotted in Fig.13. Concerning the reference incidence $i = 4°$, a fairly good prediction of the experimental results is achieved. This follows the good prediction of the contours previously

observed in Fig.12. For $z/h > 0.25$, only the blade wake contributes to the losses, and the level is low. For $z/h < 0.25$, more intense losses are induced by the corner separation. The LB simulation yields a very good prediction of the evolution along z, in particular the extent of the corner separation. The levels, which are particularly sensitive to the reference pressure P_{in}, are slightly under-estimated. When the incidence increases to $i = 7°$, the losses in the blade wake are little affected in the experiment, but they increase in the simulation. This mis-prediction could be due to the wall-function and the moderate resolution of the boundary layer. Nevertheless, concerning the corner separation, its evolution is properly captured by the simulation: it develops moderately along z.

The analysis of the results at the reference incidence $i = 4°$, and their evolution at $i = 7°$, in comparison with the experiment, have shown that the present LB methodology can capture the corner separation and its sensitivity (at these two angles of attack). Now, the simulation is going to be used to analyze a parameter that was not investigated experimentally: the incoming boundary layer thickness. Indeed, in the experiment, the incoming boundary layer is thick ($\delta/c = 0.2$ at 'station 2'), but it can be thin in compressors. In the next subsection, the simulation will be used to analyze the influence of this parameter.

4.2 Incoming boundary-layer thickness

In order to reduce the incoming boundary layer thickness, the inflow plane is moved closer to the blade (at 0.447 m) and the end-wall trip height is reduced to 1 mm. The resulting characteristics of the boundary-layer at 'station 2' are given in Table 2. The thicknesses are 3 to 5 times smaller than in the reference case, depending on which thickness definition is used. This is significantly thinner. Moreover, the turbulent regime is confirmed by the value of the shape factor: $H_{12} = 1.41$.

The influence of the thinner boundary layer on the corner separation is investigated in Fig. 14, where the total pressure loss coefficient downstream of the blade is shown. The corner separation is still present, as shown by the triangular loss region at low z/h, but its spanwise (z-) extent is reduced compared to the reference case. This reduction is natural since one of the driving mechanisms of corner separation, the incoming boundary layer, is reduced. However, it is quite remarkable that corner separation still persists.

The pitchwise averaged loss coefficient is shown in Fig. 15. As expected, the losses in

the wake of the blade ($z/h > 0.25$) are identical, but the spanwise extent of the corner-separation wake is reduced.

4.3 Wall function

Wall modelling is a popular way to reduce computational effort in large-eddy simulations of high Reynolds-number flows [29]. The use of a wall function in the vicinity of the walls allows greater cell sizes and time steps. This is particularly advantageous with Cartesian grids, generally employed by LB methods, since the cell has only one characteristic length, controlled by the minimal length requirement. However, the wall function must be able to adapt to the complex situations that can be encountered in the flow (e.g. three-dimensional velocity profiles, boundary-layer separation). The formulation used in the present study appears particularly effective in capturing the corner separation, as shown in section 3. The behavior of the wall function is investigated more closely in the present section by analyzing the influence of each term of the model.

Three additional simulations are performed at $i = 4°$, activating gradually the pressure-gradient term and the curvature term of the wall function (see formulation in section 2.2.1):

- both the pressure-gradient and the curvature corrections are deactivated (simulation labeled 'no correction term');
- only the pressure-gradient term is activated (simulation labeled 'grad(P) term only')
- only the curvature term is activated (simulation labeled 'curv. term only')

These simulations are compared to the simulation, introduced in section 3, where both the pressure-gradient and the curvature correction terms are activated (simulation labeled 'complete wall function').

The total pressure losses downstream of the blade are shown in Fig. 16, and the pitchwise average is presented in Fig. 17. In this section, the complete wall function case is considered as a reference. It was shown in good agreement with the experiment (see Fig. 12 and Fig. 13), and the measurement plots are not repeated for clarity purpose.

First, when both correction terms are deactivated, the results are notably deteriorated compared to the reference case with the complete wall function. The wake of the blade is thickened at midspan, due to the separation of the suction-side boundary-layer. This

results from a delayed transition to turbulence in the suction-side boundary layer: at $z/h = 0.38$ and $s^* = 0.5$, the maximum value of the normalized tangential velocity fluctuation is 0.03, compared to 0.15 in the reference case. Conversely, the corner separation is reduced, in both size and intensity. Surprisingly, losses are also reduced above the corner separation wake ($z/h \sim 0.15$), perhaps under the influence of the two separations (suction side and corner). These observations are confirmed by the pitchwise integration: losses are increased near midspan, but reduced in the corner separation and in the blade wake just above.

When the pressure-gradient term is activated, there is little effect in the corner separation wake, but the results are further deteriorated in the blade wake. The boundary-layer separation on the blade suction-side increases and the pitchwise integrated losses are greater.

Activating only the curvature term is much more beneficial. There is no more separation on the suction side of the blade and the integrated losses in the blade wake compare to the reference case. Furthermore, the corner separation develops, but remains smaller and less intense than in the experiment or the reference simulation.

The best results are obtained when both corrections are activated. The curvature correction promotes the transition to turbulence and allows a proper description of the boundary layer on the suction side, but the pressure correction must be added to improve the description of the corner separation. The corner separation is a more complex phenomenon, because of the interaction of two boundary layers (blade suction-side and casing). The boundary layer on the casing is thick but develops on a flat wall. Its behavior is affected by the pressure gradient induced by the blade.

Conclusion

Lattice-Boltzmann large-eddy simulations have been presented on a configuration of industrial interest: a corner separation flow in a blade cascade, at representative Reynolds number and low Mach number. The LB approach is rather new in the context of internal flows in turbomachinery and the following benefits have been highlighted in the present case: the immersed-boundary method allows a rapid quasi-autonomous meshing of the domain, and the LB methodology combined with a wall-modelling strategy reduce the computation cost by a raw factor of 300 compared to a previous wall-resolved finite-

volume compressible Navier-Stokes simulation. This comparison, rectified to equivalent number of cells and time step, still gives a gain in computational efficiency by a factor of 5 in favour of the LB approach.

A good prediction of the reference case (4° incidence) has been achieved. This is remarkable because this configuration is known to be particularly difficult to simulate, as demonstrated by previous failed attempts with RANS models. Moreover, the sensitivity of the separation to the incidence angle (4° to 7°) is also in agreement with the experiment.

This fidelity of the method, and the very limited computational cost, offered the opportunity to investigate the influence of the incoming boundary layer thickness. This parameter is of practical interest and could not be investigated experimentally. The results of the LB simulations confirm the physical expectation: a notable reduction of the boundary layer thickness results in a smaller corner separation. However, it is worth noting the separation is not completely suppressed.

The good description of this complex separated flow, by relying on a wall function to represent the inner part of the boundary layer, is noteworthy. This shows the capabilities of this strategy. Furthermore, the behaviour of the present formulation of the wall function has been analysed, by running simulations with selected combinations of terms. It is shown that the curvature term has a dominant effect, by promoting the transition to turbulence on the blade suction side and preventing a spurious separation away from the end-wall. In addition to this term, the pressure-gradient term allows a wider corner separation to develop, in better agreement with the experimental results. It probably describes more effectively the influence of the blade pressure-gradient on the end-wall boundary layer. These observations are valuable for future applications of the methodology to complex flows.

Future work should consider higher Mach numbers, in order to investigate the performance (computational efficiency and fidelity) of the LB methods adapted to these conditions.

Nomenclature

CFD	Computational Fluid Dynamics
LB	Lattice Boltzmann
LBM	Lattice Boltzmann method
LES	large-eddy simulation
RANS	Reynolds-averaged Navier-Stokes
f_i	particle distribution
$\mathbf{c_i}$	particle velocity
Ω_i	collision operator
τ_S	collisional relaxation coefficient
c_s	sound speed
ν	kinematic viscosity
C_p	pressure coefficient
c	chord length (150 mm)
c_a	axial chord length
H_{12}	boundary-layer shape factor
h	total blade span (370 mm)
i	incidence angle
P_0	total pressure
s^*	normalized curvilinear coordinate
$\mathbf{U}$	mean velocity
U_0	inflow velocity
$\mathbf{u}'$	fluctuating velocity
u_w	friction velocity
δ	boundary-layer thickness
δ_1	displacement thickness
δ_2	momentum thickness
ω_t	total pressure loss coefficient
ω_t^*	pitchwise-averaged loss coefficient
p	pressure
ρ	density

Acknowledgments

Feng Gao, Benoit Bonnal and Ignacio Gonzalez-Martino are gratefully acknowledged for providing us the comparison data. Simulations have been performed at École Centrale de Lyon on local HPC facilities (PMCS2I) supported by the Auvergne-Rhône-Alpes region (GRANT CPRT07-13 CIRA) and the national Equip@Meso grant (ANR-10-EQPX-29-01). H. T. and E. L. acknowledge the financial support of BPIFrance (Project CLIMB No. P3543-24000) in the framework of the program "Investissement d'Avenir: Calcul Intensif et Simulation Numérique".

References

[1] Zambonini, G., Ottavy, X., and Kriegseis, J., 2017. "Corner Separation Dynamics in a Linear Compressor Cascade". *Journal of Fluids Engineering,* **139**(6), pp. 061101–061101–13.

[2] Gao, F., Ma, W., Zambonini, G., Boudet, J., Ottavy, X., Lu, L., and Shao, L., 2015. "Large-eddy simulation of 3-D corner separation in a linear compressor cascade". *Physics of Fluids (1994-present),* **27**(8), p. 085105.

[3] Gao, F., Ma, W., Sun, J., Boudet, J., Ottavy, X., Liu, Y., Lu, L., and Shao, L., 2017. "Parameter study on numerical simulation of corner separation in LMFA-NACA65 linear compressor cascade". *Chinese Journal of Aeronautics,* **30**(1), pp. 15–30.

[4] Xia, G., Medic, G., and Praisner, T. J., 2018. "Hybrid RANS/LES Simulation of Corner Stall in a Linear Compressor Cascade". *Journal of Turbomachinery,* **140**(081004).

[5] Higuera, F. J., Succi, S., and Benzi, R., 1989. "Lattice gas dynamics with enhanced collisions". *Europhysics Letters (EPL),* **9**(4), pp. 345–349.

[6] Sagaut, P., 2010. "Towards advanced subgrid models for lattice-boltzmann-based large-eddy simulation: theoretical formulation". *Computers and Mathematics with Applications,* **59**(2194-2199).

[7] Maros, A., Bonnal, B., Gonzalez-Martino, I., Kopriva, J., and Polidoro, F., 2020. "Corner Stall Prediction in a Compressor Linear Cascade Using Very Large Eddy Simulation Lattice-Boltzmann Method". *Journal of Turbomachinery,* **142**(7). Publisher: American Society of Mechanical Engineers Digital Collection.

[8] Pope, S. B., 2000. *Turbulent Flows*. Cambridge University Press.

[9] Grad, H., 1949. "On the kinetic theory of rarefied gases". *Commun. Pure Appl. Maths,* **2**(4), pp. 331–407.

[10] Shan, X., and He, X., 1998. "Discretization of the velocity space in the solution of the Boltzmann equation". *Phys. Rev. Lett.,* **80**, pp. 65–68.

[11] Shan, X., Yuan, X.-F., and Chen, H., 2006. "Kinetic theory representation of hydrodynamics: a way beyond the navier-stokes equation". *J. Fluid Mech.,* **550**(1), p. 413.

[12] Bhatnagar, P., Gross, E., and Krook, M., 1954. "A model for collision processes in gases. I. small amplitude processes in charged and neutral one-component systems". *Phys. Rev.,* **94**(3), p. 511.

[13] Ricot, D., Marié, S., Sagaut, P., and Bailly, C., 2009. "Lattice boltzmann method with selective viscosity filter". *Journal of Computational Physics,* **228**(12), pp. 4478 – 4490.

[14] Leveque, E., Touil, H., Malik, S., Ricot, D., and Sengissen, A., 2018. "Wall-modeled large-eddy simulation of the flow past a rod-airfoil tandem by the Lattice Boltzmann method". *International Journal of Numerical Methods for Heat & Fluid Flow,* **28**(5, SI), pp. 1096–1116.

[15] Hosseini, S. A., Coreixas, C., Darabiha, N., and Thévenin, D., 2019. "Stability of the lattice kinetic scheme and choice of the free relaxation parameter". *Phys. Rev. E,* **99**, p. 063305.

[16] Latt, J., and Chopard, B., 2006. "Lattice boltzmann method with regularized pre-collision distribution functions". *Math. Comput. Simul.,* **72**, pp. 165–168.

[17] Krüger, T., Kusumaatmaja, H., Kuzmin, A., Shardt, O., Silva, G., and Viggen, E. M., 2016. *The Lattice Boltzmann Method: Principles and Practice*. Springer.

[18] Verschaeve, J. C. G., and Müller, B., 2010. "A curved no-slip boundary condition for the lattice boltzmann method". *J. Comput. Phys.,* **228**, pp. 4478–4490.

[19] Grad, H., 1949. "On the kinetic theory of rarefied gases". *Communications on Pure and Applied Mathematics,* **2**(4), pp. 331–407.

[20] Malaspinas, O., and Sagaut, P., 2014. "Wall model for large-eddy simulation based on the lattice boltzmann method". *Journal of Computational Physics,* **275**, p. 25–40.

[21] Patel, V. C., and Sotiropoulos, F., 1997. "Longitudinal curvature effects in turbulent boundary layer". *Prog. Aerospace Sci.,* **33 (1-2)**, pp. 1–70.

[22] Afzal, N., 1996. "Wake layer in a turbulent boundary layer with pressure gradient: A new approach". *IUTAM Symposium on Asymptotic Methods for Turbulent Shear flows at High Reynolds Numbers,* **535**, pp. 95–118.

[23] Tardu, F. S., and Maestri, R., 2010. "Wall shear stress modulation in a turbulent flow subjected to imposed unsteadiness with adverse pressure gradient". *Fluid Dynamics Research,* **42**(3).

[24] Malaspinas, O., and Sagaut, P., 2014. "Wall model for large-eddy simulation based on the lattice boltzmann method". *Journal of Computational Physics,* **275**, pp. 25 – 40.

[25] Lévêque, E., Toschi, F., Shao, L., and Bertoglio, J.-P., 2007. "Shear-improved smagorinsky model for large-eddy simulation of wall-bounded turbulent flows". *J. Fluid Mech.,* **570**, pp. 491–502.

[26] Cahuzac, A., Boudet, J., Borgnat, P., and Lévêque, E., 2010. "Smoothing algorithms for mean-flow extraction in large-eddy simulation of complex turbulent flows". *Phys. Fluids,* **22**, p. 125104.

[27] Touil, H., Ricot, D., and Lévêque, E., 2013. "Direct and large-eddy simulation of turbulent flows on composite multi-resolution grids by the lattice boltzmann method". *Journal of Computational Physics,* **256**, pp. 220–233.

[28] Gao, F., 2014. "Advanced numerical simulation of corner separation in a linear compressor cascade". PhD thesis, Ecole Centrale de Lyon.

[29] Frére, A., Sørensen, N. N., Hillewaert, K., and Winckelmans, G., 2016. "Discontinuous galerkin methodology for large-eddy simulations of wind turbine airfoils". *Journal of Physics: Conference Series,* **753**, p. 022037.

	u_w [m/s]	δ [mm]	$\delta_1 = \delta^*$ [mm]	$\delta_2 = \theta$ [mm]	H_{12} [.]
Exp.	1.45	30.0	3.7	2.8	1.32
LBM	1.52	26.4	3.7	2.7	1.34

Table 1: Inflow boundary-layer parameters at 'station 2', where u_w is the friction velocity, δ is the boundary-layer thickness, δ_1 is the displacement thickness, δ_2 is the momentum thickness and H_{12} is the boundary-layer shape factor.

	u_w [m/s]	δ [mm]	$\delta_1 = \delta^*$ [mm]	$\delta_2 = \theta$ [mm]	H_{12} [.]
LBM $i = 4°$	1.52	26.4	3.7	2.7	1.34
LBM $i = 4°$ thin BL	1.88	8.4	0.8	0.6	1.41

Table 2: Inflow boundary layer parameters at 'station 2'.

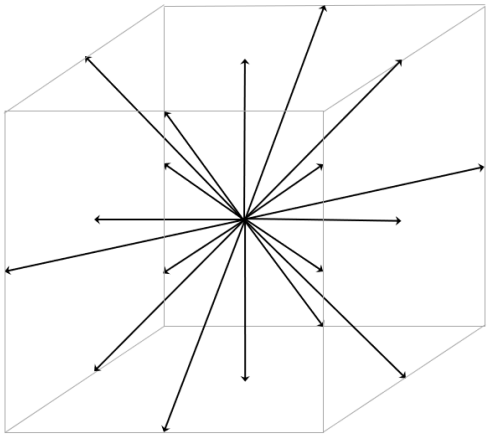

Figure 1: Set of microscopic velocities (in lattice units) at each node of the D3Q19 lattice.

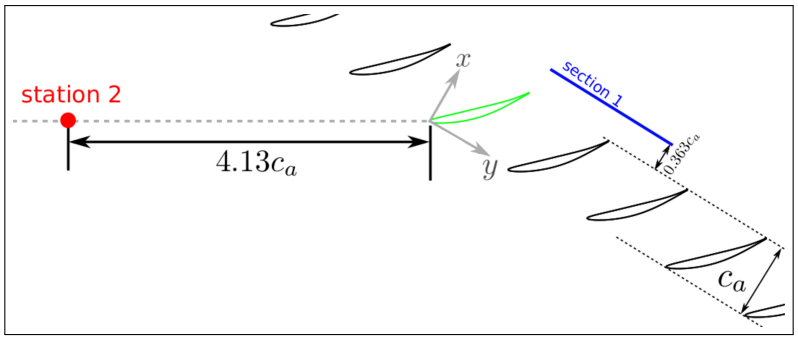

Figure 2: ECL blade cascade configuration. The incoming boundary layer is investigated at 'station 2' and the losses at 'section 1'.

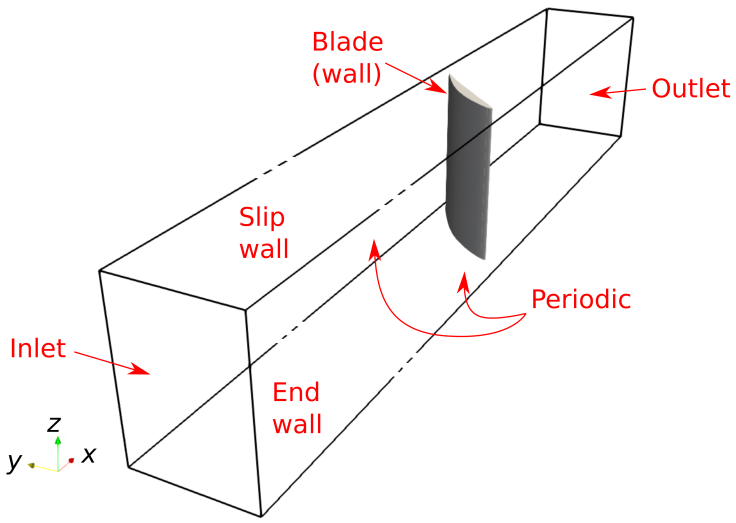

Figure 3: Computational domain ; the inflow channel has been shortened for visualization purpose.

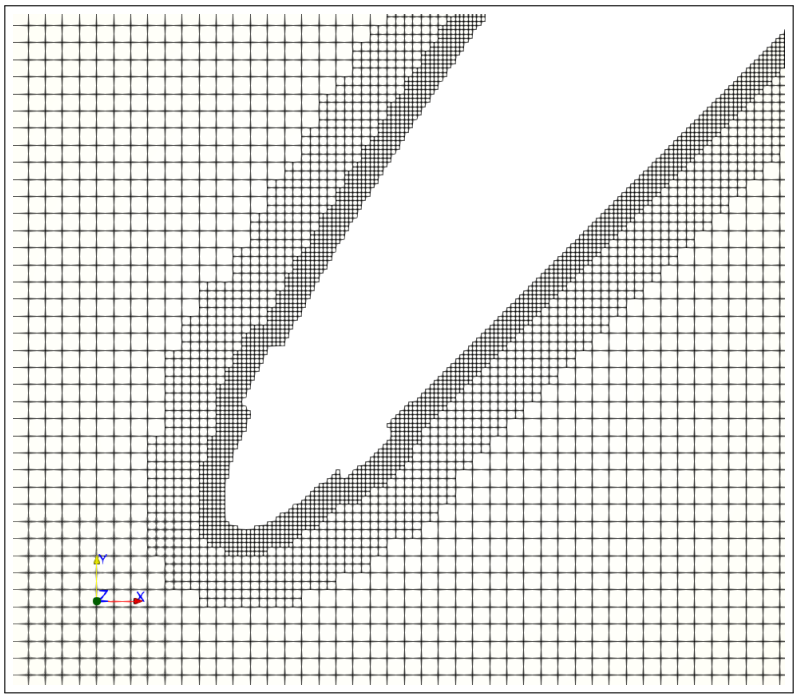

Figure 4: Mesh around the leading edge of the blade, at mid-span.

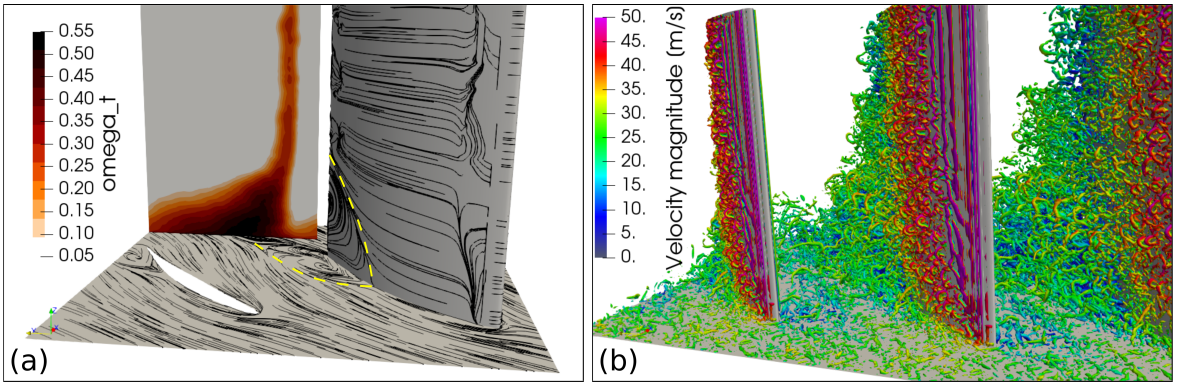

Figure 5: (a): mean flow in the reference case; friction lines on end-wall and blade suction side, and total pressure loss coefficient ω_t at 'section 1'. The yellow dashed lines indicate the corner separation. (b): instantaneous isosurface of Q-criterion, colored by velocity magnitude. Both views are from the upstream side.

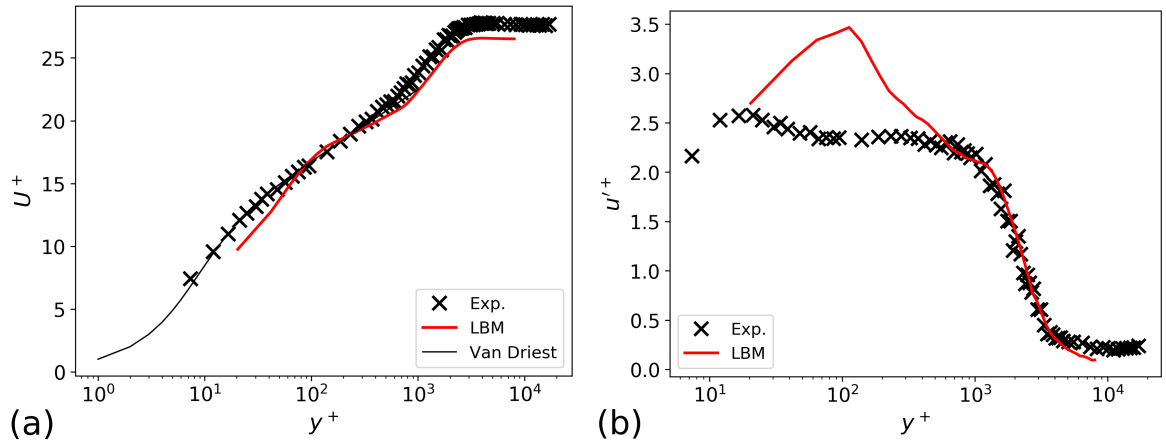

Figure 6: Mean (a) and fluctuating (b) velocity profiles at 'station 2' (inflow boundary layer).

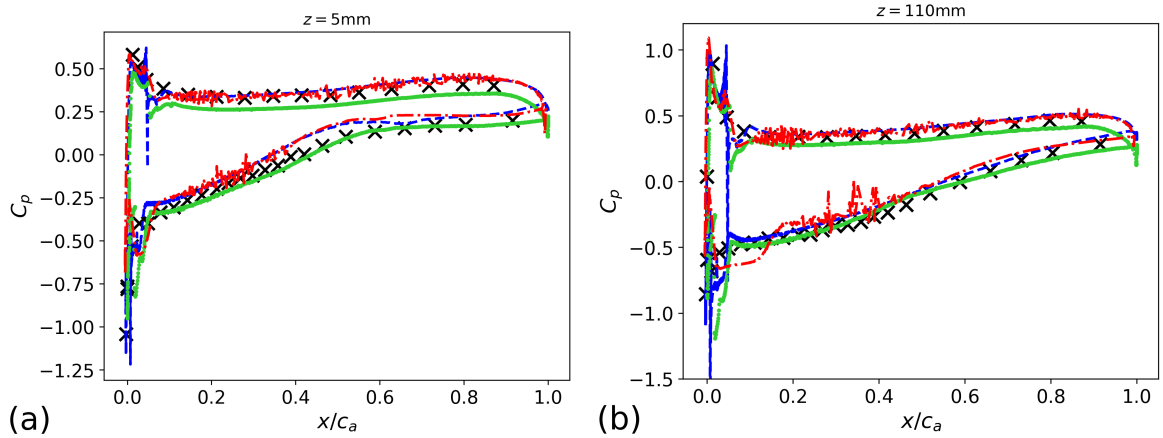

Figure 7: Wall pressure coefficient on the blade, at (a): $z = 5\,\text{mm}$ ($z/h = 1.4\%$), and (b): $z = 110\,\text{mm}$ ($z/h = 29.7\%$). ×: experiment, – – – : Gao *et al.*, ——— : Maros *et al.*, – · – : present LB simulation.

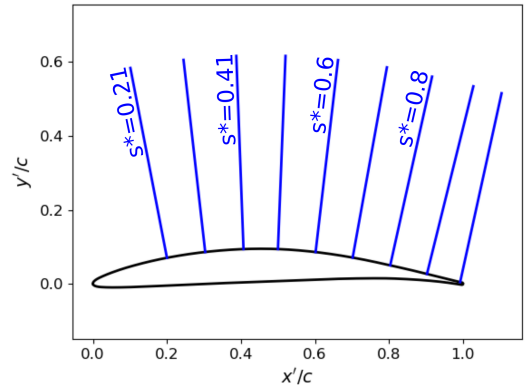

Figure 8: Positions of the velocity profiles on the blade.

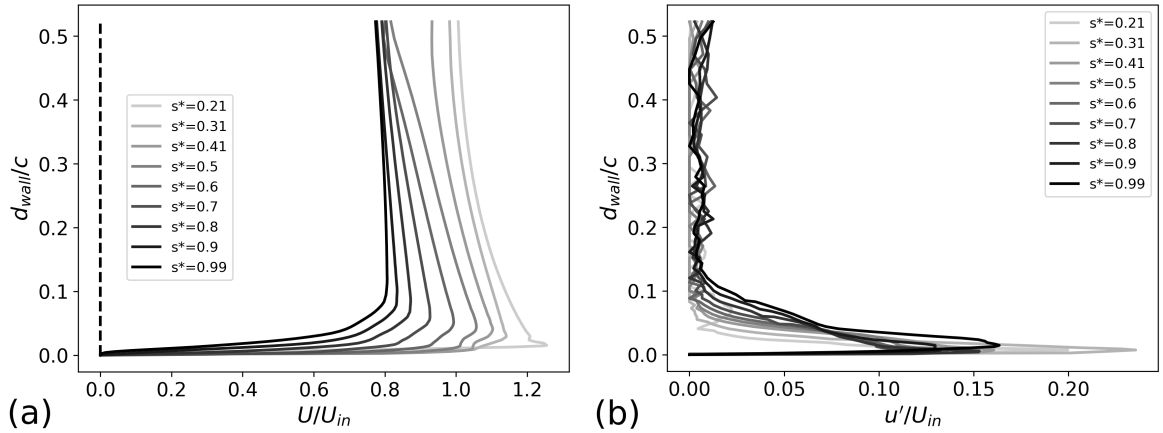

Figure 9: Mean (a) and fluctuating (b) tangential velocities on suction side, at $z/h = 29.7\%$. s^* is the normalized curvilinear coordinate along suction side (0: leading edge, 1: trailing edge), d_{wall} is the distance to the suction side.

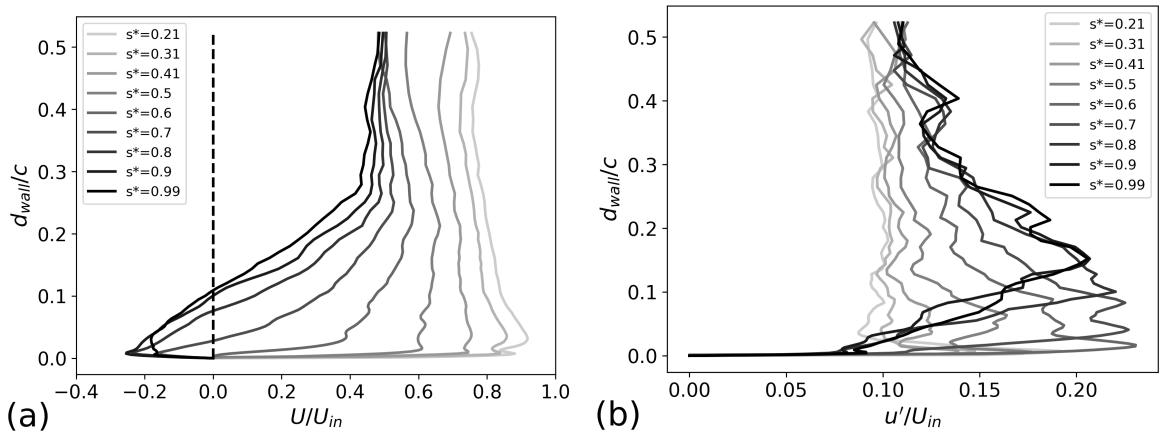

Figure 10: Mean (a) and fluctuating (b) tangential velocities on suction side, at $z/h = 1.4\%$. s^* is the normalized curvilinear coordinate along suction side (0: leading edge, 1: trailing edge), d_{wall} is the distance to the suction side.

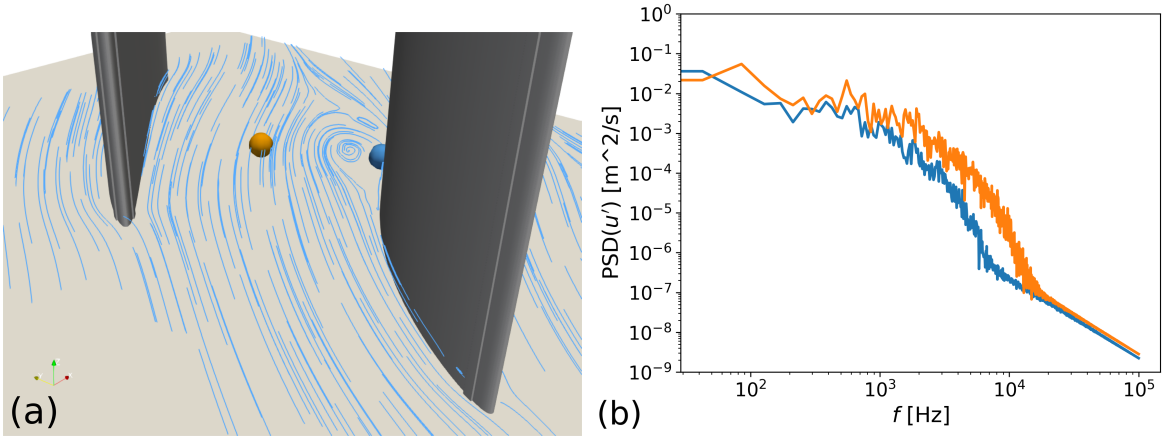

Figure 11: Power-spectral density of u' at two positions near the end-wall. (a): probe locations, (b): spectra.

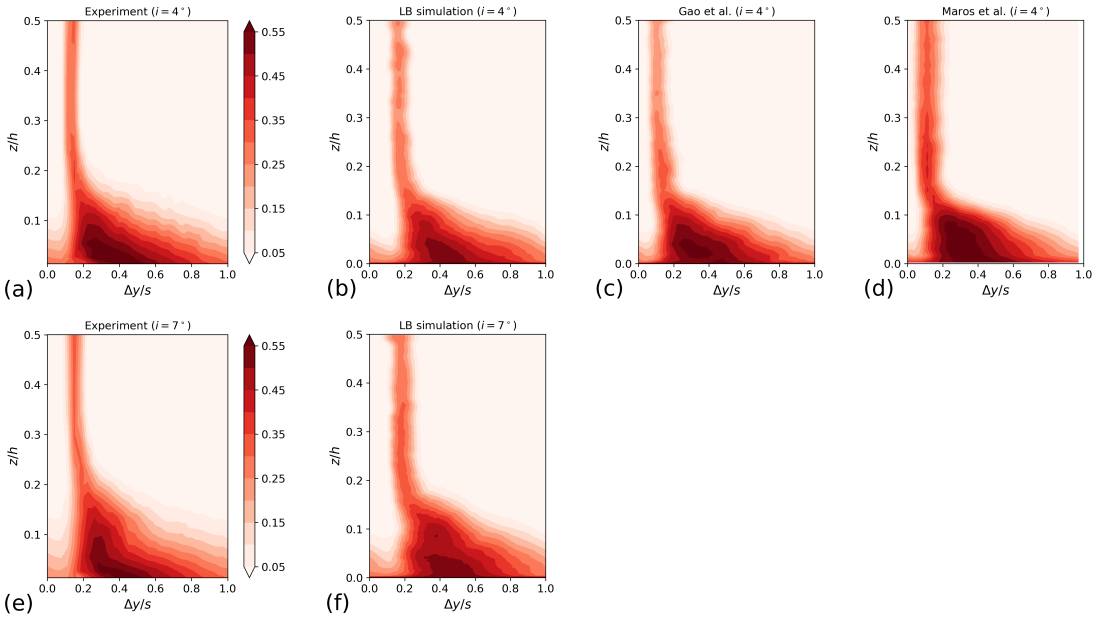

Figure 12: Total pressure loss coefficient ω_t at 'section 1', $0.363\,c_a$ downstream of the trailing edge. Top: $i = 4°$, bottom: $i = 7°$. (a) & (e): experiment, (b) & (f): LB simulation, (c) LES results courtesy of Gao *et al.* [2], (d) LB results courtesy of Maros *et al.* [7].

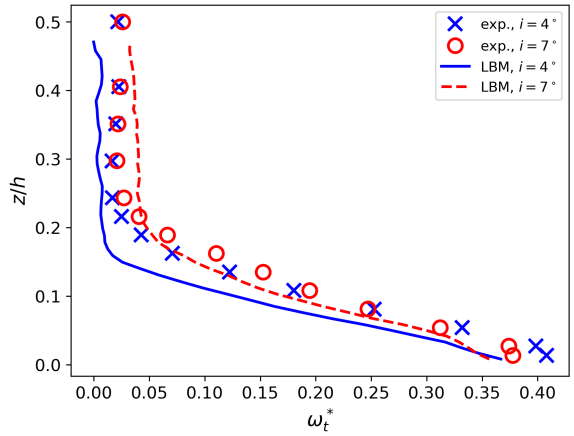

Figure 13: Pitchwise-averaged loss coefficient ω_t^*, at 'section 1'.

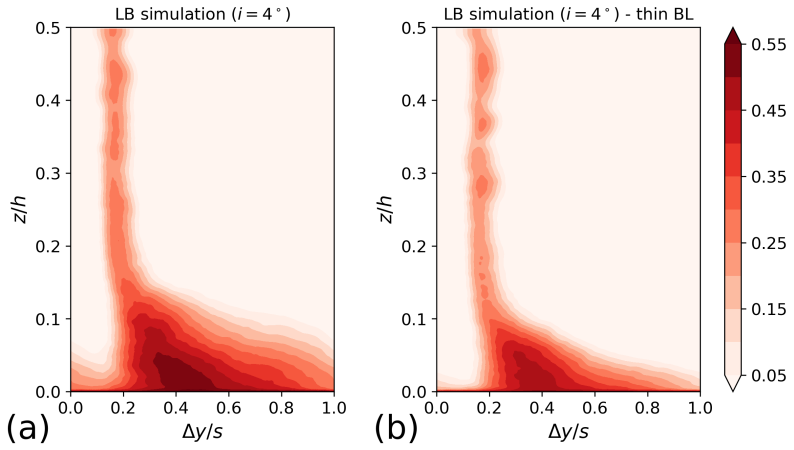

Figure 14: Total pressure loss coefficient ω_t at 'section 1', $0.363\,c_a$ downstream of the trailing edge. (a): LBM $i = 4°$, (b): LBM $i = 4°$ thin boundary layer.

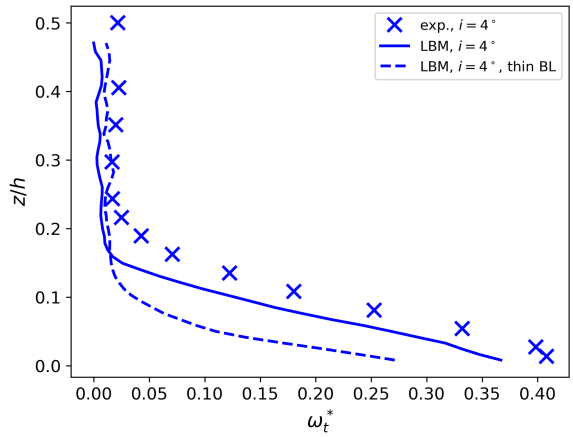

Figure 15: Pitchwise-averaged loss coefficient ω_t^*, at 'section 1'.

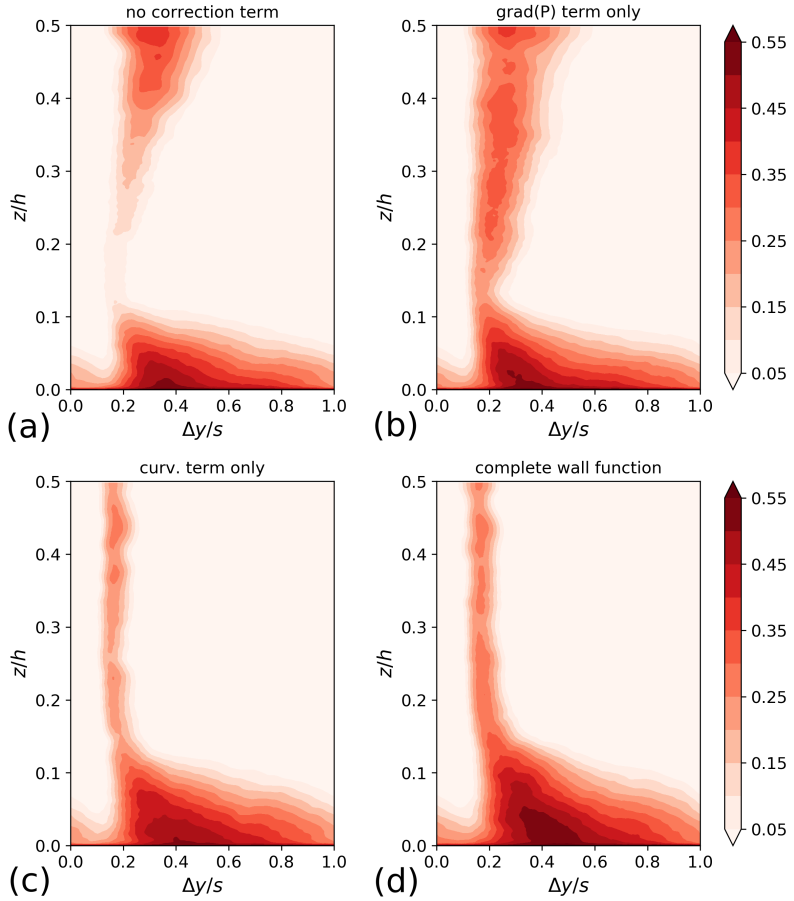

Figure 16: Total pressure loss coefficient ω_t at 'section 1', at distance $0.363\,c_a$ downstream of the trailing edge, $i = 4°$. Influence of the wall function terms. (a): no correction term, (b): pressure-gradient term only, (c): curvature term only, (d): complete wall function.

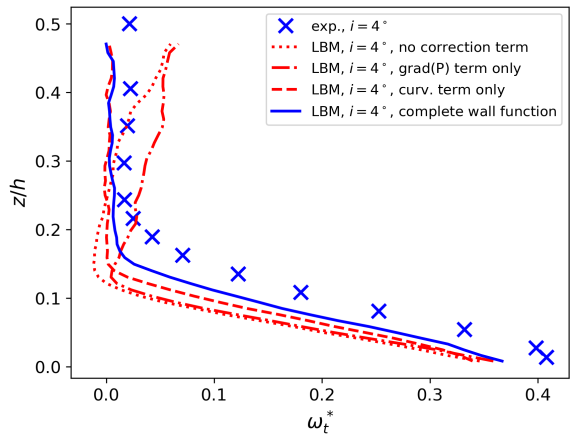

Figure 17: Pitchwise-averaged loss coefficient ω_t^*, at 'section 1'. Influence of the wall function terms.